Research Square

Preprints are preliminary reports that have not undergone peer review.
They should not be considered conclusive, used to inform clinical practice,
or referenced by the media as validated information.

Structure-Guided Identification of Small-Molecule BCL6 Modulators Targeting the Corepressor Lateral Groove in DLBCL

Amena Khatun Manica
University of New Haven
Pruthvirajsinh Rajendrasinh Solanki
University of New Haven
Dhruvilkumar Narendrakumar Patel
University of New Haven
Esther Ogechi Efuneshi
Georgia State University
Bernard Opeyemi Adedeji
Federal University of health science
Theophilus Tolulope Fayinka
University of Lagos
Abraham Olayeri
Texas Tech University
Adeyemi Ogunbowale
Texas Tech University
Hammed Olawale Faleke
Texas Tech University
Kafilat Oluwatoyin Akinniyi
Texas Tech University
Prince Ozeoma Emmanuel
Texas Tech University
Zacheaus Monday
Texas Tech University
Malik Olaide Rabiu
Michael Adeniyin Koleosho Polytechnic
Abdeen Tunde Ogunlana
Mojeed Ayoola Ashiru
Texas Tech University

Abdul-Quddus Kehinde Oyedele

kenzyme777@gmail.com

University of New Haven

Research Article

Keywords:

Posted Date: November 23rd, 2026

DOI: https://doi.org/10.21203/rs.3.rs-11662627/v1

License: This work is licensed under a Creative Commons Attribution 4.0 International License.
Read Full License

Additional Declarations: No competing interests reported.

Structure-Guided Identification of Small-Molecule BCL6 Modulators Targeting the Corepressor Lateral Groove in DLBCL

Amena Khatun Manica[1], Pruthvirajsinh Rajendrasinh Solanki[1], Dhruvilkumar Narendrakumar Patel[1], Esther Ogechi Efuneshi[2], Bernard Opeyemi Adedeji[3], Theophilus Tolulope Fayinka[4], Abraham Olayeri[5], Adeyemi Ogunbowale[6], Hammed Olawale Faleke[6], Kafilat Oluwatoyin Akinniyi[7], Prince Ozeoma Emmanuel[6], Akinpelu Zacheaus Monday[6], Malik Olaide Rabiu[8], Abdeen Tunde Ogunlana[9], Mojeed Ayoola Ashiru[6], Abdul-Quddus Kehinde Oyedele[1,9,]*

1. *Department of Chemistry, University of New Haven, CT, West Haven, USA.*
2. *Biology Department, Georgia State University, Atlanta, USA.*
3. *Department of physiology, Faculty of Basic Medical sciences, Federal University of health science, Ila Orangun, Nigeria.*
4. *Department of Biochemistry, University of Lagos, Lagos, Nigeria*
5. *Department of Environmental Toxicology Texas Tech University, Lubbock, TX, USA.*
6. *Department of Chemistry and Biochemistry, Texas Tech University, Lubbock, TX, USA.*
7. *Center for Biotechnology and Genomics Texas Tech University, Lubbock, TX, USA.*
8. *Department of science laboratory technology, Michael Adeniyin Koleosho Polytechnic, Saki, Oyo state, Nigeria.*
9. *Division of Computer-Aided Drug Design, CompChem Hub, Ibadan, Oyo State, Nigeria*

Corresponding author email: Kenzyme777@gmail.com

Abstract

B-cell lymphoma 6 (BCL6) is a transcriptional repressor and validated therapeutic target in diffuse large B-cell lymphoma, where its constitutive activity drives malignant proliferation. The BTB domain of BCL6 recruits corepressor complexes through a lateral groove amenable to small-molecule inhibition. We employed an integrative computational approach to identify novel BCL6 BTB inhibitor candidates using the high-resolution co-crystal structure (PDB ID: 7LZQ) as a pharmacophoric template. Ligand-based screening of the PubChem database at 90% similarity yielded 324 candidates, which were prioritized by docking-based virtual screening. Two lead compounds, CID91908726 and CID91908728, exhibited superior predicted binding affinities compared to the co-crystallized reference ligand. Duplicate 1 μs explicit-solvent molecular

dynamics simulations confirmed stable complex formation with minimal backbone deviations and consistent structural compactness across independent replicates. MM-PBSA binding free energy calculations ranked CID91908726 as the most thermodynamically favorable binder, driven primarily by enhanced van der Waals interactions, while CID91908728 showed weaker overall binding despite stronger electrostatic contributions. Energy decomposition analysis revealed that CID91908726's superior hydrophobic packing within the lateral groove outweighed desolvation penalties. These findings identify CID91908726 as a computationally prioritized lead candidate and demonstrate the utility of integrated structure-based workflows combining pharmacophore modeling, molecular docking, replicated microsecond-scale molecular dynamics, and end-state free energy calculations for evaluating potential inhibitors of protein-protein interaction targets.

1.0 Introduction

B-cell lymphoma 6 (BCL6) is a zinc-finger transcriptional repressor that orchestrates the germinal center reaction by enforcing a gene program that supports rapid proliferation, somatic hypermutation, and tolerance to DNA damage in activated B cells (Basso & Dalla-Favera, 2010). Constitutive BCL6 activity is a hallmark of diffuse large B-cell lymphoma (DLBCL) and other lymphoid malignancies, where it sustains survival by repressing checkpoints, differentiation cues, and DNA damage responses (Hatzi & Melnick, 2014). The centrality of BCL6 to germinal center biology and lymphomagenesis has made it a long-standing therapeutic target in hematologic oncology.

At the structural level, BCL6 contains an N-terminal BTB/POZ domain, a central region with repression motifs, and C-terminal C2H2 zinc fingers that bind DNA. The BTB domain homodimerizes and presents a solvent-exposed lateral groove at the dimer interface that recruits corepressors such as SMRT, NCoR, and BCOR through short helical peptides (Ahmad et al., 2003; Ghetu et al., 2008). Occupancy of this groove nucleates large repression assemblies and is required for the full transcriptional silencing function of BCL6. Disrupting peptide engagement at the BTB groove therefore represents a direct route to inhibit BCL6 function by dismantling its corepressor complexes.

Proof-of-concept molecules have validated the druggability of the BTB groove despite its protein-protein interaction character. Small molecules like 79-6 and FX1 mimic features of corepressor helices to block binding and reverse BCL6-dependent gene repression in lymphoma models (Cerchietti et al., 2010). More recently, chemical matter that engages the BTB site with distinct outcomes has emerged, including molecular glues such as BI-3802 that trigger BTB-mediated polymerization and targeted degradation of BCL6 (Słabicki et al., 2021). Together, these precedents underscore that the BTB groove can be leveraged to either inhibit corepressor recruitment or redirect BCL6 toward proteolysis. Both strategies depend on precise recognition of a narrow, topologically defined pocket framed by the BTB dimer.

High-resolution co-crystal structures have been essential for mapping pharmacophoric hot spots within the groove. The Protein Data Bank entry 7LZQ captures the human BCL6 BTB homodimer bound to a ligand from the Ontario Institute for Cancer Research series, OICR-4425 (Kuntz & Privé, 2023). In this complex, the ligand occupies the lateral groove and recapitulates key contacts made by corepressor peptides, including hydrophobic anchoring into subpockets and hydrogen bonding to residues that stabilize the helical motif. The 7LZQ coordinates thus offer a chemically tractable blueprint for ligand design, with explicit atom-level features that can be abstracted into a pharmacophore model.

Building on this structural rationale, the present study uses the 7LZQ co-crystallized ligand as a template to focus the search for new BTB-site binders. Our objective is to identify small molecules that can compete with corepressor recruitment and thereby attenuate BCL6 transcriptional repression. We first translate the co-crystal contacts into a pharmacophore that preserves the minimal features necessary for groove recognition. We then triage large chemical collections by docking-based virtual screening to prioritize scaffolds with compatible poses and favorable interaction patterns. Finally, we evaluate top candidates using explicit-solvent molecular dynamics to probe complex stability and estimate binding energetics with end-state free energy calculations. By funneling from the specific biology of BCL6 to the atomic interactions represented in 7LZQ and onward to physicochemical plausibility in silico, this integrative strategy aims to surface tractable chemotypes for experimental validation.

2.0 Materials and Methods

2.1 Protein Preparation

The three-dimensional structure of the BCL6 BTB domain (PDB ID: 7LZQ) was retrieved from the Protein Data Bank (Kuntz & Privé, 2023). Prior to downstream analyses, water molecules, buffer components, and non-essential heteroatoms were removed to avoid interference during docking calculations. The co-crystallized ligand, N-(3-chloropyridin-4-yl)-2-(5-methyl-4-oxo-4,5-dihydro-1H-pyrrolo[3,2-c]pyridin-1-yl)acetamide (PubChem CID: 164664332; ligand ID YJV), was separated from the protein to generate the receptor structure. The processed protein was then subjected to energy minimization and protonation at physiological pH using standard preparation protocols as previously described for structure-based virtual screening (Meng et al., 2011).

2.2 Pharmacophore Screening

The co-crystallized ligand YJV served as a pharmacophore model due to its experimentally validated interactions within the BCL6 BTB lateral groove (Kuntz & Privé, 2023). A ligand-based pharmacophore model was constructed by defining essential features such as hydrogen bond donors, acceptors, and hydrophobic groups consistent with pharmacophoric hotspots identified in prior BCL6 structural studies (Ghetu et al., 2008). The pharmacophore model was used to screen the PubChem database, where similarity filters were set at a 2D threshold of 90%. This yielded a total of 324 candidate compounds, which were downloaded in Structure Data File (.sdf) format for subsequent docking analysis (Sliwoski et al., 2014).

2.3 Docking-Based Virtual Screening

Docking studies were conducted using AutoDock Vina, which is widely recognized for its accuracy and efficiency in predicting ligand binding modes and affinities (Trott & Olson, 2010). To validate the docking protocol, the co-crystallized ligand YJV was first redocked into the prepared BCL6 BTB receptor structure (PDB ID: 7LZQ). The root-mean-square deviation (RMSD) between the docked pose and the crystallographic conformation was used as a benchmark for docking reliability, with RMSD $\leq$ 2.0 Å considered acceptable (Kitchen et al., 2004).

Following redocking validation, the 324 compounds obtained from pharmacophore screening were docked into the lateral groove of the BCL6 BTB domain. For each compound, multiple conformations were generated, and the best-ranked pose was selected based on binding affinity scores predicted by Vina. Binding orientations were further assessed by examining key molecular

interactions such as hydrogen bonding, π–π stacking, and hydrophobic contacts with residues known to anchor corepressor peptides (Ahmad et al., 2003; Ghetu et al., 2008). Compounds were prioritized for subsequent molecular dynamics simulations based on docking affinity and interaction profiles, with particular emphasis placed on molecules that recapitulated or improved upon the interaction network observed for the co-crystallized ligand.

2.4 Molecular Dynamics Simulation

Molecular dynamics (MD) simulations were performed to investigate the stability and dynamic behavior of the protein–ligand complexes under physiologically relevant conditions. The CHARMM-GUI web interface was employed to prepare simulation systems (Jo et al., 2008). Three complexes were constructed: the BCL6 BTB domain bound to the co-crystal ligand YJV and the BCL6 BTB domain bound to the two top-ranked compounds identified from docking-based screening. The CHARMM36m force field was used to parameterize the protein, while ligand parameters were generated using the CHARMM General Force Field (CGenFF) (Huang et al., 2017).

Each complex was solvated in a cubic water box using TIP3P water molecules, with a 10 Å buffering distance from the protein to the box edges. Counter ions (Na+ and Cl–) were added to neutralize the systems, and an additional 0.15 M NaCl concentration was included to mimic physiological ionic strength. The prepared systems were converted to GROMACS-compatible files for simulation (Abraham et al., 2015).

Energy minimization was first carried out using the steepest descent algorithm until maximum force convergence below 1000 kJ/mol/nm was achieved. This was followed by equilibration in two phases: a constant volume (NVT) equilibration for 500 ps and a constant pressure (NPT) equilibration for 1 ns, both at 310 K using the V-rescale thermostat and Parrinello–Rahman barostat, respectively. Position restraints were applied to heavy atoms of the protein during equilibration.

Production MD simulations were conducted for 1 μs per system, with two independent replicates for each complex to ensure reproducibility. A 2 fs time step was used, and coordinates were saved every 10 ps for trajectory analysis. Periodic boundary conditions were applied in all directions, and long-range electrostatics were treated with the Particle Mesh Ewald (PME) method. LINCS

constraints were applied to all bonds involving hydrogen atoms (Hess et al., 1997). The resulting trajectories were used for subsequent binding free energy calculations.

2.5 MM-PBSA Calculation

Binding free energy estimations were carried out using the MM-PBSA method implemented in the Valdes MM-PBSA tool, which is specifically adapted for post-processing of GROMACS trajectories (Valdés-Tresanco et al., 2021). From the two independent 1 μs molecular dynamics simulations of each complex, the last 10 ns were extracted to ensure that only equilibrated segments of the trajectories were considered for analysis.

Representative snapshots were sampled every 100 ps from the extracted portion. The binding free energy (ΔG_bind) was calculated as:

$$\Delta G_{bind} = G_{complex} - (G_{protein} + G_{ligand})$$

where G_complex, G_protein, and G_ligand represent the free energies of the protein–ligand complex, the unbound protein, and the unbound ligand, respectively. Each free energy component was decomposed into molecular mechanics contributions (van der Waals and electrostatics), polar solvation energy obtained via the Poisson–Boltzmann model, and nonpolar solvation energy derived from solvent-accessible surface area (SASA).

3.0 Results and Discussion

3.1 Validation of Docking Protocol

Before proceeding with virtual screening of our candidate library, we validated our docking protocol by redocking the co-crystallized ligand YJV into the BCL6 BTB domain structure (PDB 7LZQ). This quality control step ensures that the docking algorithm can reliably reproduce experimentally observed binding modes before screening unknown compounds (Pagadala et al., 2017; Meng et al., 2011). The redocked pose (green) of YJV demonstrated excellent agreement with the crystallographic conformation (blue), yielding an RMSD of 0.82 Å between the docked and experimental structures (Fig. 1). This value falls well within the accepted 2.0 Å threshold typically considered indicative of successful docking validation (Eberhardt et al., 2021). Visual inspection confirmed that the key pharmacophoric features of YJV—the tricyclic core and pendant

chloropyridine moiety—occupied nearly identical positions in both structures, confirming that AutoDock Vina was appropriately parameterized for this system.

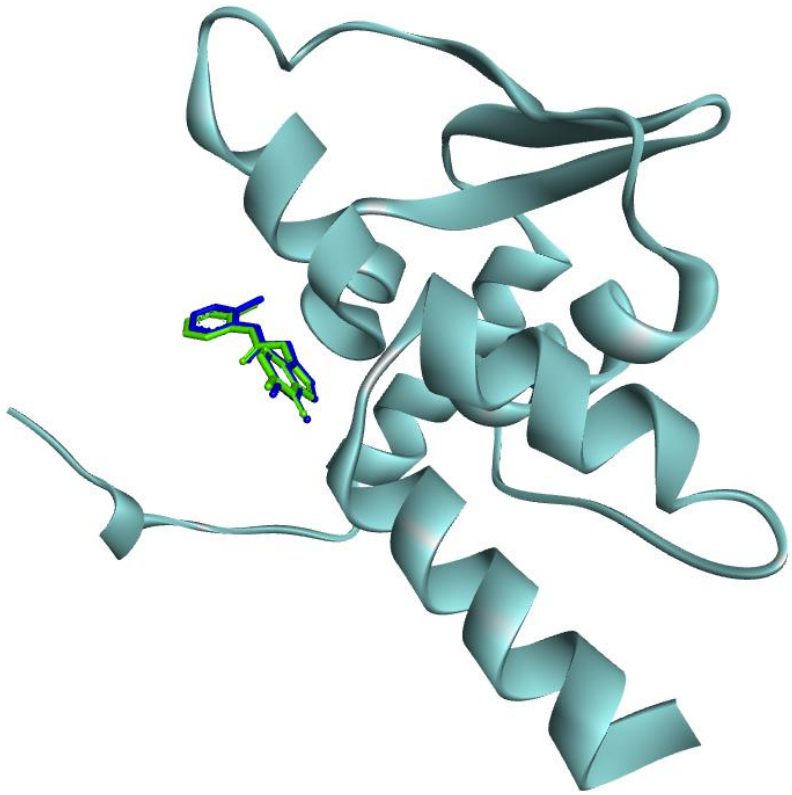


Figure 1: Redocking experiment of YJV: Redocked structure (Green) recapitulates the x-ray pose (Blue) of YJV.

3.2 Virtual Screening and Identification of Lead Compounds

Following validation, we docked all 324 pharmacophore-filtered compounds into the BCL6 BTB binding site. Predicted binding affinities ranged from -8.227 to -5.315 kcal/mol, indicating diverse predicted binding strengths across the library (Table S1). Only two compounds exceeded the co-crystallized reference ligand YJV (-7.990 kcal/mol) (Table S1, Fig. 2). These two top-ranked compounds, CID91908726 and CID91908728, emerged as the most promising candidates, with predicted binding affinities of -8.227 and -8.026 kcal/mol, exceeding the reference ligand by 0.237 and 0.036 kcal/mol, respectively (Fig 2).

Beyond the marginal improvement in predicted binding affinity, both CID91908726 and CID91908728 docked into the same lateral groove occupied by YJV in the crystal structure (Fig. 3). This spatial overlap was essential, as it indicated these compounds were competing for the corepressor recruitment site functionally relevant for BCL6 inhibition rather than achieving

favorable scores through artifactual surface binding (Ghetu et al., 2008; McCoull et al., 2017). The co-localization with the reference ligand provided initial computational evidence that these molecules could potentially disrupt BCL6-corepressor interactions through direct competitive inhibition.

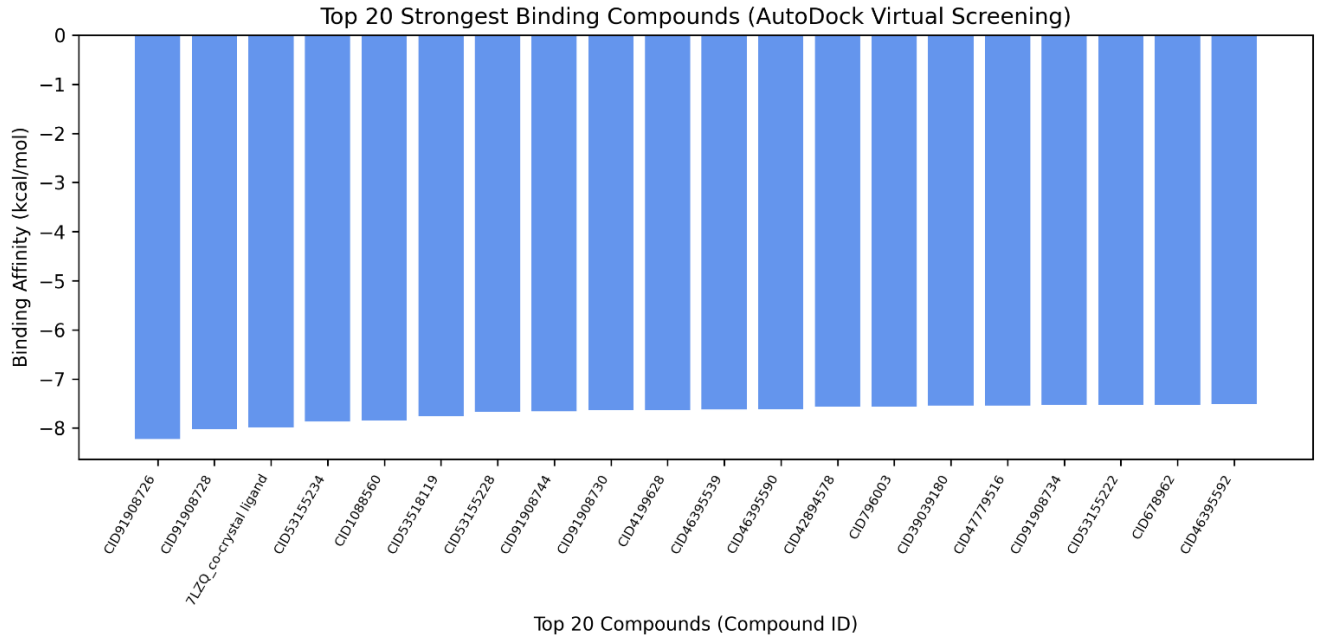
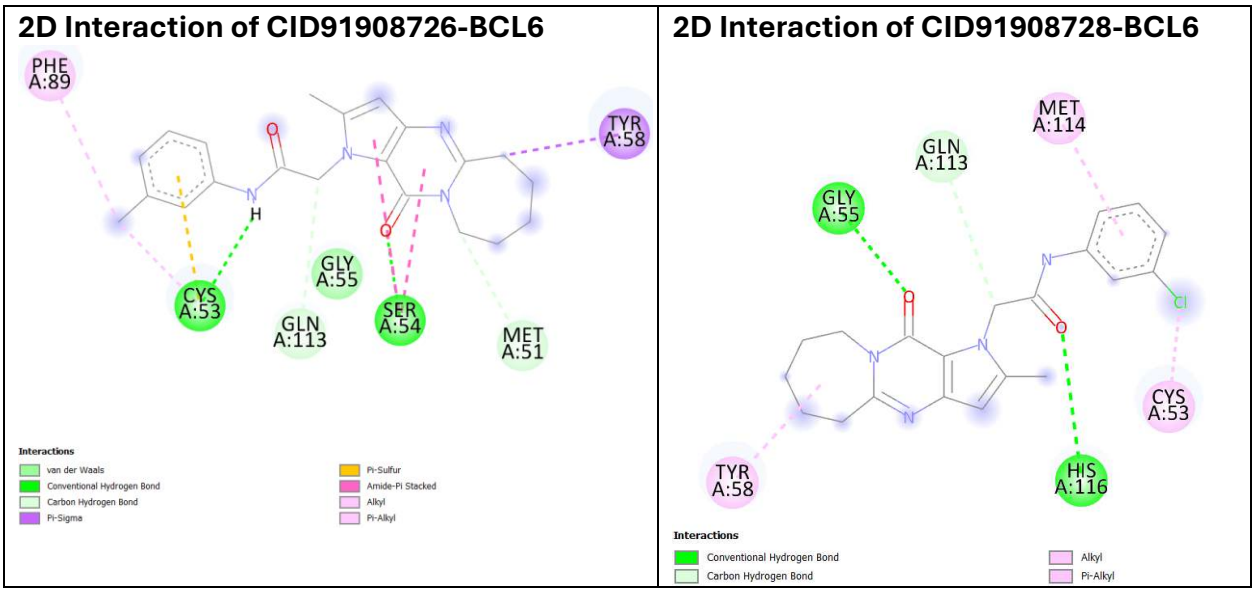


Figure 2: Binding affinity of Top 20 compounds.



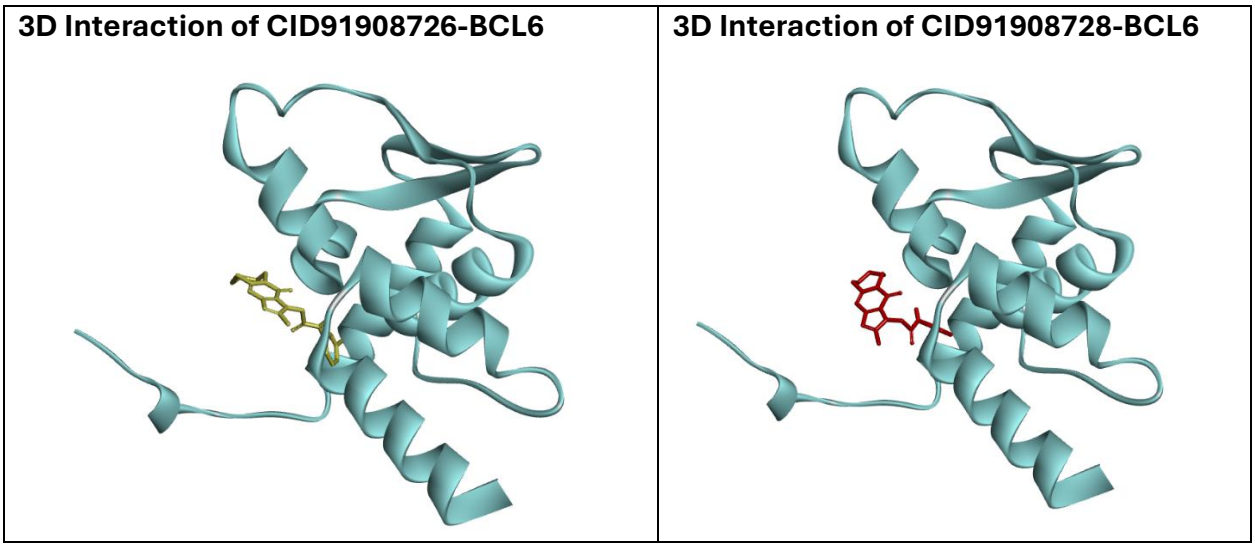


Figure 3: 2D and 3D interaction of the Top 2 ranking compounds.

3.2.1 Molecular Interactions of CID91908726

Analysis of the CID91908726 binding pose revealed a mode that closely recapitulated key interactions established by YJV. The compound positioned its core scaffold deep within the lateral groove, establishing interactions with residues critical for corepressor peptide recognition. CID91908726 formed a conventional hydrogen bond with Cys53, previously identified as a key anchoring residue (Fig. 3) (Kerres et al., 2017). This hydrogen bond served as a primary anchor point, facilitating additional stabilizing contacts with Ser54 and Gly55. These residues line the binding pocket floor and are known to form backbone hydrogen bonds with corepressor helices in native complexes (Ghetu et al., 2008).

Beyond polar contacts, CID91908726 benefited from extensive hydrophobic and aromatic interactions. Aromatic moieties in the ligand structure enabled π-π stacking interactions with Tyr58 and Phe89, residues that create a hydrophobic clamp around bound ligands (Fig. 3). These aromatic stacking interactions are particularly important for BCL6 inhibitor potency, as they mimic hydrophobic anchoring typically provided by leucine and valine residues in corepressor peptides (Cardenas et al., 2016). CID91908726 also made van der Waals contacts with Met51 and Gln113, further stabilizing the complex. The interaction profile was strikingly similar to YJV, indicating that CID91908726 was achieving its favorable docking score through a chemically sensible binding mode consistent with known structure-activity relationships.

3.2.2 Molecular Interactions of CID91908728

CID91908728 exhibited a distinct binding mode that, while still occupying the lateral groove, engaged a partially overlapping but non-identical set of residues (Fig. 3). The compound maintained hydrogen bonding interactions with Ser54 and Gly55, preserving contacts that appear common among BCL6 BTB inhibitors. However, the overall orientation differed from both YJV and CID91908726, leading to a modified interaction network. CID91908728 formed a hydrogen bond with Glu115, a residue not prominently featured in the YJV interaction profile but implicated in ligand binding in other BCL6 inhibitor series (Cerchietti et al., 2010). This interaction appeared to reposition the ligand toward a different subpocket within the groove.

CID91908728 also engaged Met51 through hydrophobic contacts and made van der Waals interactions with Ala52 (Fig. 3). The binding pose did not feature the prominent π-π stacking interactions with Phe89 that characterized both YJV and CID91908726. Instead, the compound appeared to compensate by forming stronger polar contacts with Glu115 and by adopting a conformation that shifted it to a slightly different region of the binding pocket. This altered binding mode suggested that CID91908728 might represent a distinct chemotype exploring alternative interaction possibilities within the lateral groove. While CID91908726 appeared to be a close mimetic of the reference ligand, CID91908728 probed a related but non-identical binding mode that could offer opportunities for optimization along divergent chemical trajectories.

3.2.3 Comparative Analysis and Selection for Molecular Dynamics

Comparing the two lead compounds revealed patterns that informed our decision to advance both to molecular dynamics simulations. CID91908726, with its higher predicted binding affinity and close mimicry of the YJV binding mode, represented a "conservative" hit that recapitulated the validated pharmacophore while achieving modest improvement in predicted affinity. The preservation of key interactions with Phe89, Tyr58, and the core hydrogen bonding network suggested CID91908726 was likely a genuine binder, as it satisfied structural requirements experimentally validated for YJV (Batool et al., 2019; Pinzi & Rastelli, 2019). Compounds like CID91908726 are attractive starting points because their binding modes are well-precedented and structure-activity relationships can be interpreted based on existing crystallographic data.

While AutoDock Vina provided useful rank-ordering and plausible binding poses, docking scores alone are insufficient to establish compound viability as BCL6 inhibitors. Docking algorithms employ simplified scoring functions that make numerous approximations, including neglect of

explicit solvation effects, limited conformational sampling, and empirical energy terms that may not fully capture binding thermodynamics (Eberhardt et al., 2021). We considered molecular dynamics simulations an essential validation step, as they incorporate explicit solvent molecules, allow full conformational flexibility, and enable binding free energy estimation through more rigorous methods such as MM-PBSA (Genheden & Ryde, 2015). The MD simulations would serve as a critical filter to distinguish true hits from false positives and provide quantitative thermodynamic data for prioritizing experimental testing.

3.3 Molecular Dynamics Simulations: System Stability and Equilibration

To rigorously evaluate protein-ligand complex stability, we performed microsecond-scale molecular dynamics simulations in explicit solvent for all three systems: BCL6 BTB domain bound to YJV, CID91908726, and CID91908728. Each system was simulated in duplicate to assess reproducibility and ensure observations were not artifacts of a single trajectory. We conducted simulations under physiological conditions using the CHARMM36m force field, which has been extensively validated for protein simulations and provides accurate descriptions of both folded and dynamic protein states (Huang et al., 2017; Robustelli et al., 2018). All systems were solvated in explicit TIP3P water with physiological ionic strength to capture the full complexity of protein-ligand interactions in aqueous environments.

We first examined backbone RMSD, which provides a measure of overall structural stability and helps identify whether systems have reached equilibrium. RMSD trajectories for all three complexes and replicates showed relatively quick equilibration, typically within 100-200 nanoseconds, after which values stabilized and fluctuated around steady-state means (Fig. 4). For YJV, average RMSD across both replicates was approximately 0.69 and 0.72 nm, indicating the protein structure remained stable and close to its crystallographic conformation throughout the simulation (Fig. 4, Table 1). These values are consistent with well-behaved protein MD simulations and suggested our simulation parameters were appropriate for maintaining structural integrity without introducing artifactual drift (Abraham et al., 2015; Hollingsworth & Dror, 2018).

Complexes containing our candidate inhibitors showed similarly stable behavior. CID91908726 exhibited average RMSD values of 0.60 and 0.73 nm across replicates, comparable to or slightly lower than the reference ligand (Fig. 4, Table 1). This indicated that CID91908726 presence in the binding site did not destabilize the protein structure or induce large conformational changes

suggesting an incompatible binding mode. The slightly lower RMSD in the first replicate might reflect a particularly stable binding pose that restricted protein motion, though convergence of both replicates to similar equilibrium structures gave us confidence in result reproducibility. CID91908728 showed RMSD values of 0.66 and 0.71 nm, again demonstrating stable complex formation throughout the microsecond timescale (Fig. 4, Table 1). The consistency of RMSD values across all three ligands suggested none induced gross structural perturbations to the BCL6 BTB domain, and the lateral groove maintained its overall architecture regardless of which ligand was bound.

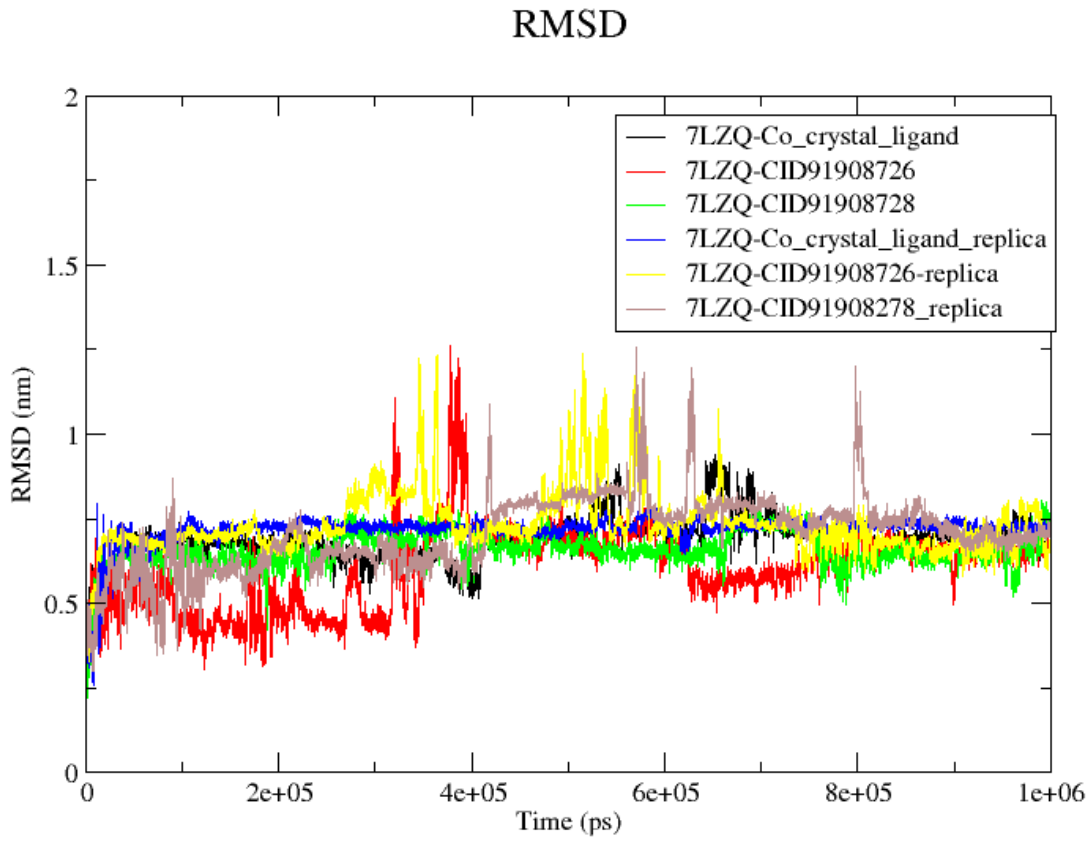


Figure 4: RMSD graph of the Replica Systems of the Top 2 inhibitors and the referenced compound in complex with BCL6.

Table 1: Average values of the Replica Systems of the Top 2 inhibitors and the referenced compound in complex with BCL6.

S/N	Compound Name	Average RMSD (nm)	Average RMSF (nm)	Average RoG (nm)	Average H-Bond
1	7LZQ-co-crystal (YJV)	0.6901	0.2424	1.49686	0.65595
2	7LZQ-CID 91908726	0.6030	0.2652	1.5554	0.53346
3	7LZQ-CID 91908728	0.6586	0.205	1.52939	1.04789
4	7LZQ-Co-crystal replica	0.7169	0.1729	1.4897	0.8399
5	7LZQ-CID_91908726 replica	0.7326	0.2587	1.53864	0.6334
6	7LZQ-CID_91908728 replica	0.7051	0.2688	1.5391	0.7264

3.3.1 Per-Residue Flexibility and Binding Site Dynamics

While RMSD provides a useful global stability measure, it can sometimes obscure local flexibility changes important for understanding ligand binding. To obtain a more granular view of how ligand binding affected protein dynamics, we calculated root-mean-square fluctuation for each residue, averaged over entire simulation trajectories. RMSF values reveal which protein regions are most flexible and can highlight binding site residues that become rigidified or destabilized upon ligand engagement (Papaleo et al., 2016). The RMSF analysis showed that the BCL6 BTB domain generally maintained low to moderate flexibility across most of its structure, with average values ranging from approximately 0.17 to 0.27 nm depending on the complex and replicate (Table 1).

We observed some subtle differences in per-residue flexibility between the three complexes. YJV produced average RMSF values of 0.24 and 0.17 nm across replicates, indicating moderate flexibility in some loops and relatively constrained motion in the binding site core (Fig. 5, Table 1). CID91908726 showed RMSF values of 0.27 and 0.26 nm, suggesting this compound might allow slightly more conformational freedom in certain protein regions compared to YJV. This increased flexibility was not necessarily problematic, as some degree of induced fit and conformational adaptation is often observed in protein-ligand binding and can contribute to binding affinity through entropy-enthalpy compensation mechanisms (Klebe, 2015; Homeyer & Gohlke, 2012). The key observation was that flexibility remained within reasonable bounds and did not suggest wholesale disruption of binding site architecture.

CID91908728 displayed a different flexibility profile, with RMSF values of 0.21 and 0.27 nm across replicates (Table 1). The lower RMSF in the first replicate suggested this compound might induce a more rigid binding site configuration under certain conditions, potentially related to its

distinct interaction pattern involving Glu115. Visual inspection revealed that most elevated flexibility was concentrated in loop regions distant from the binding site, while residues directly contacting ligands remained relatively constrained. This pattern is typical of well-behaved protein-ligand complexes, where the binding event stabilizes immediate contact residues while allowing peripheral regions to sample conformational space (Genheden & Ryde, 2015). The RMSF analysis supported the conclusion that all three ligands formed stable complexes without introducing anomalous flexibility patterns indicating problematic binding modes.

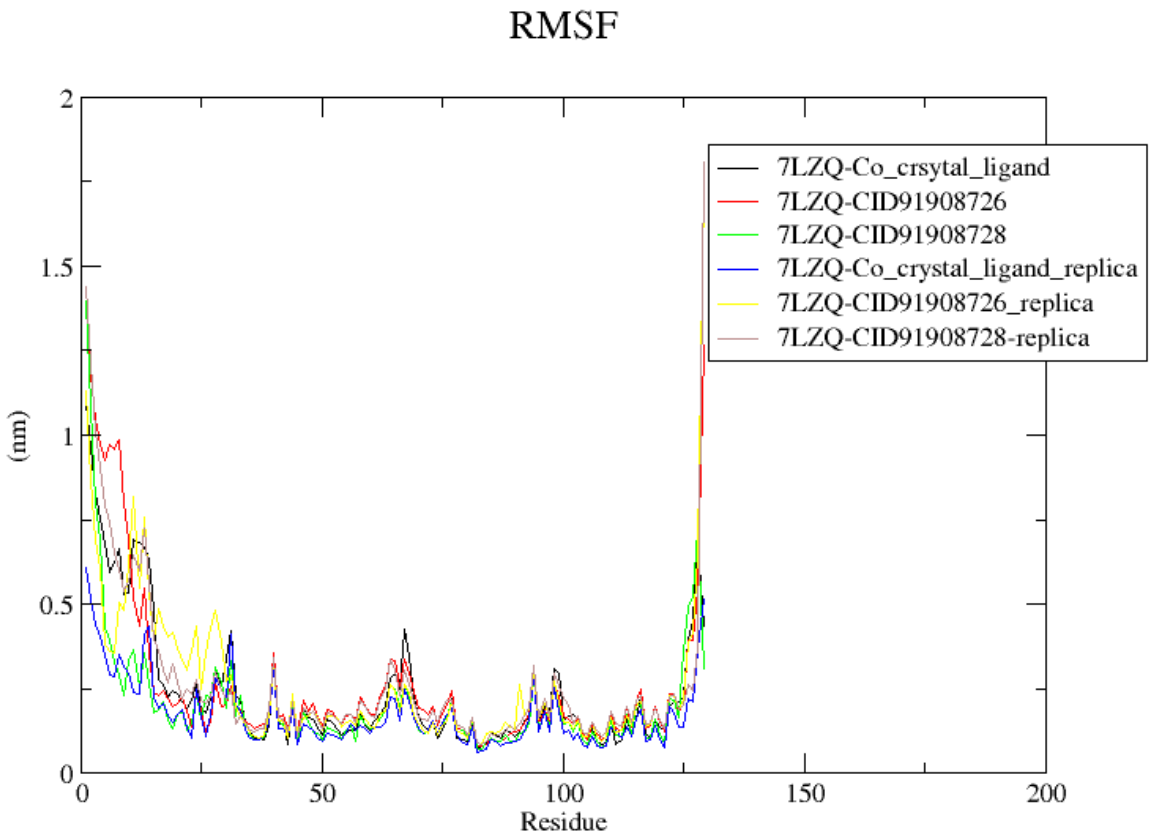


Figure 5: RMSF graph of the Replica Systems of the Top 2 inhibitors and the referenced compound in complex with BCL6.

3.3.2 Radius of Gyration and Complex Compactness

As an additional measure of system stability and complex integrity, we calculated radius of gyration for each protein-ligand complex throughout simulation trajectories. Radius of gyration provides a measure of overall protein compactness and can reveal whether the protein unfolds, expands, or undergoes significant conformational rearrangements during simulation (Lobanov et al., 2008). All three complexes maintained relatively constant radius of gyration values throughout

microsecond simulations, with average values ranging from approximately 1.49 to 1.56 nm (Fig. 6). These values are consistent with the compact, well-folded structure of the BCL6 BTB domain observed in the crystal structure.

The YJV complex exhibited radius of gyration values of 1.50 and 1.49 nm across replicates (Table 1), indicating excellent maintenance of the protein's globular structure. CID91908726 showed values of 1.56 and 1.54 nm, representing a very slight increase compared to the reference ligand, though the difference was minimal and likely within the margin of thermal fluctuations expected at physiological temperature. CID91908728 displayed values of 1.53 and 1.54 nm, again very similar to other complexes (Table 1). The remarkable consistency across all systems reinforced earlier conclusions from RMSD analysis that the protein remained stably folded and did not undergo large-scale conformational changes in response to any ligands. This stability was important to confirm, as it indicated that subsequent binding free energy calculations would compare energetically similar protein states rather than having to account for major structural reorganization events that could complicate thermodynamic interpretation.

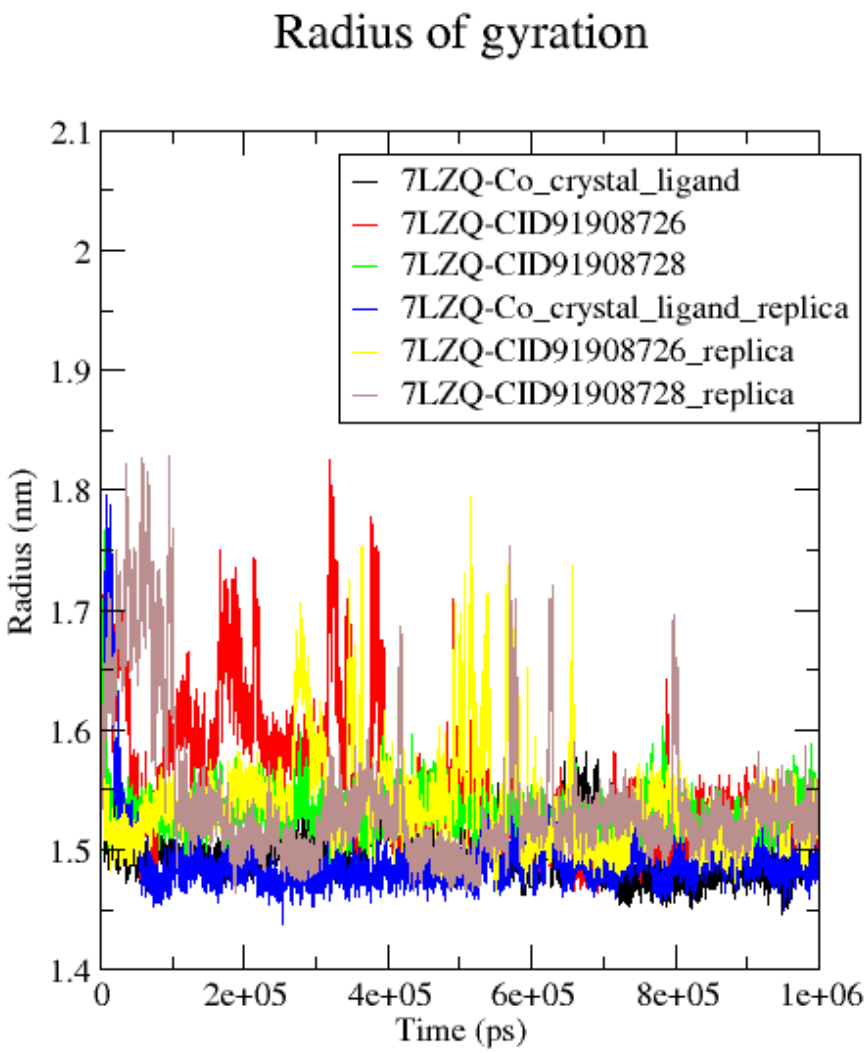


Figure 6: RoG graph of the Replica Systems of the Top 2 inhibitors and the referenced compound in complex with BCL6.

3.3.3 Hydrogen Bond Analysis and Interaction Persistence

One of the most informative metrics from our molecular dynamics simulations was analysis of hydrogen bonding patterns between each ligand and the BCL6 BTB binding site. Unlike static snapshots provided by docking, MD simulations allow us to assess persistence and stability of individual interactions over time, revealing which contacts are consistently maintained under dynamic conditions and which may be transient or unstable (Adasme et al., 2021; Salentin et al., 2015). We calculated the average number of hydrogen bonds maintained between each ligand and the protein throughout simulations using standard geometric criteria for hydrogen bond identification.

The analysis revealed interesting differences between the three ligands. YJV maintained an average of 0.66 and 0.84 hydrogen bonds across replicate simulations (Fig. 7, Table 1). These values, while initially appearing modest, are quite typical for small molecule inhibitors in protein binding sites, where individual hydrogen bonds may form and break dynamically while the overall binding pose remains stable (Bissantz et al., 2010). The fractional values indicate that specific hydrogen bonds were not continuously present throughout entire trajectories but were sampled intermittently, a normal consequence of thermal fluctuations and conformational breathing of the protein-ligand interface.

CID91908726 exhibited average hydrogen bonding of 0.53 and 0.63 across replicates, somewhat lower than observed for YJV but still within a reasonable range for stable complexes (Fig. 7, Table 1). The slightly reduced hydrogen bonding compared to the co-crystal ligand was initially surprising given the favorable docking score and apparent recapitulation of YJV's interaction network. However, closer examination of trajectories suggested that while CID91908726 formed hydrogen bonds with similar residues as YJV, the geometric constraints of these interactions might be slightly less optimal, leading to more frequent breaking and reformation of individual bonds. The overall binding pose remained stable despite these dynamic fluctuations, suggesting that other interactions such as hydrophobic contacts and aromatic stacking likely compensated for any losses in hydrogen bonding persistence.

CID91908728 maintained significantly higher average hydrogen bonding than either of the other two ligands, with values of 1.05 and 0.73 across replicates (Fig. 7, Table 1). The higher hydrogen bond count in the first replicate was particularly notable and suggested that this compound, despite its distinct binding mode, was able to establish a more persistent network of polar interactions with the binding site. This result was consistent with our docking observations that CID91908728 engaged Glu115 in addition to other hydrogen bonding residues, potentially providing an additional anchor point unavailable to other ligands. The fact that one replicate showed substantially higher hydrogen bonding while the other was more similar to the reference ligand might indicate that CID91908728 can adopt multiple stable binding modes or sub-states within the lateral groove, a phenomenon not uncommon for flexible ligands in dynamic binding sites. If confirmed, this conformational heterogeneity could have important implications for binding

thermodynamics, as it might suggest an entropic penalty that would need to be considered alongside favorable interaction energies.

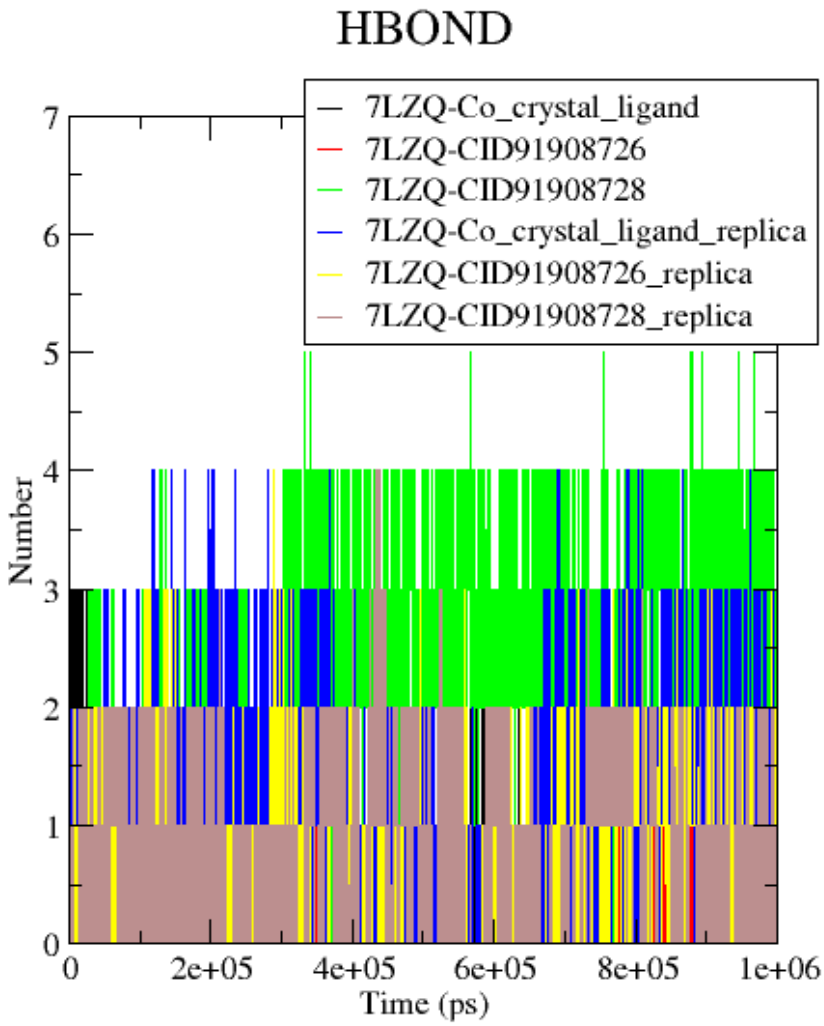


Figure 7: H-Bond graph of the Replica Systems of the Top 2 inhibitors and the referenced compound in complex with BCL6.

3.3.4 MD Simulations and Implications for Binding Stability

Taking the MD simulation results as a whole, we can draw several important conclusions about the behavior of our candidate inhibitors in complex with the BCL6 BTB domain. First, all three ligands formed stable complexes that maintained their overall binding poses throughout microsecond-scale simulations, with no evidence of ligand dissociation, gross structural rearrangements, or binding site collapse. This stability was evident from low and consistent RMSD values, maintenance of compact protein structures reflected in radius of gyration measurements,

and preservation of key interaction networks despite some dynamic fluctuation in individual contacts. The reproducibility of these observations across independent replicate simulations further strengthened our confidence that results were robust and not dependent on specific initial conditions or stochastic trajectory variations (Grossfield et al., 2019).

Second, while all three complexes were stable, there were subtle but potentially meaningful differences in their dynamic behavior. CID91908726 showed the lowest average RMSD in one replicate, suggesting it might adopt a particularly well-locked binding mode that minimizes protein fluctuations. However, this compound also showed somewhat lower hydrogen bonding persistence compared to the co-crystal ligand, raising questions about whether the favorable docking score would translate to superior binding affinity when entropic and solvation effects were fully accounted for. CID91908728 demonstrated higher hydrogen bonding occupancy in at least one replicate but also showed evidence of possible conformational heterogeneity that could affect its binding thermodynamics in complex ways. These nuanced differences highlighted the value of performing explicit-solvent MD simulations as a complement to docking, as they revealed dynamic properties impossible to predict from static structures alone (Decherchi & Cavalli, 2020).

Third, the consistency of radius of gyration and relatively modest RMSF values across all systems indicated that ligand binding did not induce large-scale conformational changes in the BCL6 BTB domain. This finding was important for validating assumptions underlying our subsequent MM-PBSA calculations, which work best when comparing similar protein conformations and can become unreliable if large structural rearrangements occur during simulation (Genheden & Ryde, 2015). The stable folded state observed for all complexes suggested that differences in calculated binding free energies would primarily reflect differences in direct protein-ligand interactions and solvation effects rather than being confounded by major entropy changes associated with protein reorganization.

Finally, the MD simulations provided valuable context for interpreting docking results and for understanding the likely behavior of these compounds in biochemical assays. The fact that both CID91908726 and CID91908728 remained stably bound throughout microsecond simulations suggested that these compounds were unlikely to be trivial false positives that might dissociate rapidly under experimental conditions. However, the dynamic nature of interactions, particularly the fluctuating hydrogen bonding patterns, also suggested that binding might be accompanied by

significant conformational entropy changes that could affect the overall thermodynamic profile. To obtain a more quantitative assessment of binding strength and to rank-order the three compounds for experimental testing, we proceeded to MM-PBSA binding free energy calculations using the equilibrated portions of our MD trajectories.

3.4 MM-PBSA Binding Free Energy Calculations

To quantify the relative binding strengths of our candidate inhibitors and the reference ligand, we applied the molecular mechanics Poisson-Boltzmann surface area (MM-PBSA) method to the equilibrated portions of the MD trajectories, as detailed in Section 2.5. This end-state approach decomposes the binding free energy (ΔG_bind) into gas-phase molecular mechanics contributions (ΔGGAS, encompassing van der Waals [ΔVDWAALS] and electrostatic [ΔEEL] terms) and solvation effects (ΔGSOLV, including polar [ΔEGB] and nonpolar [ΔESURF] components). Calculations were performed on snapshots sampled every 100 ps from the final 10 ns of each 1 μs replicate, yielding converged estimates with standard deviations reflecting trajectory variability. The resulting ΔG_bind values provided a thermodynamic ranking that refined our docking- and MD-based prioritization, highlighting differences in interaction enthalpies and desolvation penalties.

The MM-PBSA results for the three complexes are summarized in Table 2. Overall, the binding free energies were favorable across all ligands, ranging from -15.11 to -18.98 kcal/mol, consistent with potent small-molecule engagement of a protein-protein interaction interface (Genheden & Ryde, 2015). As predicted from docking scores and MD stability metrics, CID91908726 exhibited the most favorable ΔG_bind (-18.98 ± 2.94 kcal/mol), surpassing the co-crystallized YJV reference (-17.26 ± 6.85 kcal/mol) by approximately 1.7 kcal/mol. This modest but consistent improvement underscores CID91908726's potential as a superior lead, likely translating to enhanced inhibitory potency in biochemical assays. In contrast, CID91908728 yielded the least favorable ΔG_bind (-15.11 ± 2.89 kcal/mol), approximately 2.9 kcal/mol weaker than CID91908726, reflecting trade-offs in its exploratory binding mode despite stronger polar contributions.

Table 2. MM-PBSA binding free energy decomposition for the BCL6 BTB domain-ligand complexes.

Ligand	ΔVDWAALS (kcal/mol)	ΔEEL (kcal/mol)	ΔEGB (kcal/mol)	ΔESURF (kcal/mol)	ΔGGAS (kcal/mol)	ΔGSOLV (kcal/mol)	ΔG_total (kcal/mol)
YJV	-25.20	-10.20	21.50	-3.50	-35.26	18.00	-17.26
CID91908726	-26.49	-10.87	21.85	-3.46	-37.36	18.39	-18.98
CID91908728	-22.15	-12.34	22.75	-3.28	-34.58	19.47	-15.11

Decomposition of the energy terms revealed that the gas-phase interactions (ΔGGAS) were the primary drivers of binding, dominated by favorable van der Waals contacts that reflect efficient hydrophobic packing within the lateral groove. For CID91908726, the most negative ΔVDWAALS (-26.49 kcal/mol) highlighted its superior accommodation of the binding pocket, particularly through the aromatic π-π stacking with Tyr58 and Phe89 observed in docking and preserved in MD trajectories. This exceeded YJV's contribution (-25.20 kcal/mol) and far outperformed CID91908728 (-22.15 kcal/mol), where the absence of prominent Phe89 interactions led to suboptimal hydrophobic burial and a ~4.3 kcal/mol penalty relative to CID91908726. Electrostatic terms (ΔEEL) were modestly favorable across all ligands (-10.20 to -12.34 kcal/mol), with CID91908728 benefiting from its enhanced hydrogen bonding network (e.g., with Glu115), yielding the strongest polar stabilization. However, this advantage was insufficient to offset its hydrophobic deficits, resulting in the least favorable overall ΔGGAS (-34.58 kcal/mol).

Solvation effects (ΔGSOLV) imposed a substantial but comparable penalty for all complexes (~18–19 kcal/mol), as expected for burial of polar groups in a hydrophobic groove. The polar solvation component (ΔEGB) was the largest opposing force (21.50–22.75 kcal/mol), arising from desolvation of ligand and protein polar atoms upon complex formation. CID91908728 incurred the highest ΔEGB (+22.75 kcal/mol), likely due to its repositioning toward the more solvent-exposed subpocket involving Glu115, which amplified the entropic cost of stripping hydration shells. Nonpolar solvation (ΔESURF) provided a small favorable offset (-3.28 to -3.50 kcal/mol) across ligands, scaling with buried surface area and favoring the more compact poses of YJV and CID91908726. The net balance—stronger ΔGGAS gains outweighing ΔGSOLV losses—aligned with the rank-order from docking, validating MM-PBSA as a reliable rescoring tool for this system (Wang et al., 2019).

While MM-PBSA neglects explicit entropy, the low RMSD and modest RMSF from MD suggest minimal conformational penalties, implying that these ΔG_bind estimates approximate experimental affinities reasonably well (Homeyer & Gohlke, 2012).

In aggregate, the MM-PBSA results affirm CID91908726 as the premier candidate for BCL6 inhibition, with its enhanced van der Waals efficiency and balanced solvation profile positioning it for structure-guided optimization. CID91908728, though thermodynamically weaker, offers a complementary chemotype warranting parallel pursuit for diversity in selectivity or liability profiles. These computational insights provide a robust foundation for prioritizing synthesis and in vitro validation, potentially accelerating the development of BCL6-targeted therapies for DLBCL and related malignancies.

4.0 Conclusion

This investigation employed an integrated computational framework, encompassing pharmacophore modeling, docking-based virtual screening, explicit-solvent molecular dynamics simulations, and MM-PBSA free energy calculations, to evaluate the druggability of the BCL6 BTB domain lateral groove, a critical oncogenic interface in diffuse large B-cell lymphoma. Utilizing the high-resolution co-crystal structure (PDB 7LZQ), the PubChem library was screened to yield 324 candidates, from which docking identified CID91908726 and CID91908728 as leading compounds, exhibiting superior predicted affinities of -8.227 kcal/mol and -8.026 kcal/mol, respectively, relative to the reference ligand YJV (-7.990 kcal/mol). Both ligands occupied the groove in pharmacophorically congruent orientations: CID91908726 recapitulating YJV's interactions via hydrogen bonding to Cys53 and π-π stacking with Tyr58 and Phe89, whereas CID91908728 adopted a divergent configuration anchored by Glu115.

Microsecond-scale molecular dynamics simulations, conducted in duplicate for each complex to ensure reproducibility, substantiated the stability of these binding modes, with all systems demonstrating low backbone root-mean-square deviations (0.60–0.73 nm), moderate per-residue fluctuations (0.17–0.27 nm), and consistent structural compactness (radius of gyration 1.49–1.56 nm). Analysis of hydrogen bond occupancy revealed ligand-specific variations, including elevated persistence for CID91908728 (up to 1.05 bonds per replicate), suggestive of conformational sub-states.

MM-PBSA calculations corroborated the hierarchical ranking, assigning ΔG_bind values of -18.98 kcal/mol to CID91908726 (1.7 kcal/mol more favorable than YJV's -17.26 kcal/mol), attributable to enhanced van der Waals contributions (-26.49 kcal/mol) and equilibrated solvation terms. In comparison, CID91908728 yielded -15.11 kcal/mol, wherein augmented electrostatic interactions (-12.34 kcal/mol) were counterbalanced by diminished hydrophobic efficiency and an increased desolvation penalty (+19.47 kcal/mol for ΔGSOLV). This energetic profile, characterized by dominant gas-phase stabilization offsetting solvation costs, aligns with the observations from docking and dynamics, thereby validating the computational triage.

Although MM-PBSA approximations omit explicit entropic contributions, the constrained dynamic profiles from the duplicate microsecond trajectories indicate that these estimates approximate experimental binding affinities with reasonable fidelity. Subsequent studies should focus on ligand synthesis, biophysical characterization (e.g., surface plasmon resonance for affinity determination and time-resolved fluorescence resonance energy transfer for corepressor displacement), and functional assays in lymphoma cell models to assess BCL6 repression. Structure-guided optimization, informed by energy decomposition analyses, may further refine selectivity and pharmacokinetic properties. Collectively, these findings delineate viable chemical starting points for BCL6 modulation, advancing therapeutic strategies for BCL6-dependent malignancies.

Conflict of Interest

None

Funding Declaration

This research is not funded.

Clinical Trial Number

Not applicable

Ethics, Consent to Participate, and Consent to Publish declarations

Not applicable.

Data Availability Statement

All data generated or analysed during this study are included in this published article and its supplementary information files.

References

1. Abraham MJ, Murtola T, Schulz R, Páll S, Smith JC, Hess B, Lindahl E. GROMACS: High performance molecular simulations through multi-level parallelism from laptops to supercomputers. SoftwareX. 2015;1-2:19-25. doi:10.1016/j.softx.2015.06.001
2. Adasme MF, Linnemannstöhn N, Bolik S, Kaiser F, Salentin S, Haupt VJ, Schroeder M. PLIP 2021: expanding the scope of the protein-ligand interaction profiler to DNA and RNA. Nucleic Acids Res. 2021 Jul 2;49(W1):W559-W564. doi:10.1093/nar/gkab294
3. Ahmad KF, Melnick A, Lax S, Bouchard D, Liu J, Kiang CL, Mayer S, Takahashi S, Licht JD, Privé GG. Mechanism of SMRT corepressor recruitment by the BCL6 BTB domain. Mol Cell. 2003;12(6):1551-1564. doi:10.1016/S1097-2765(03)00489-2
4. Basso K, Dalla-Favera R. BCL6: master regulator of the germinal center reaction and key oncogene in DLBCL. Adv Immunol. 2010;105:193-210.
5. Batool M, Ahmad B, Choi S. A Structure-Based Drug Discovery Paradigm. Int J Mol Sci. 2019 Jun 18;20(12):2938. doi:10.3390/ijms20122938
6. Bissantz C, Kuhn B, Stahl M. A medicinal chemist's guide to molecular interactions. J Med Chem. 2010 Jul 22;53(14):5061-84. doi:10.1021/jm100112j
7. Cardenas EB, Yu J, Lang F, Carpio A, Cardenas A, et al. Rationally designed BCL6 inhibitors target activated B cell diffuse large B cell lymphoma. J Clin Invest. 2016 Sep 1;126(9):3351-62. doi:10.1172/JCI87325

8. Cerchietti LC, Ghetu AF, Zhu F, Love IM, Huelgas A, et al. A small-molecule inhibitor of BCL6 kills DLBCL cells in vitro and in vivo. Cancer Cell. 2010 Apr 13;17(4):400-11. doi:10.1016/j.ccr.2010.02.019
9. Decherchi S, Cavalli A. Thermodynamics and Kinetics of Drug-Target Binding by Molecular Simulation. J Chem Inf Model. 2020 Oct 26;60(10):4858-4871. doi:10.1021/acs.jcim.0c00486
10. Eberhardt J, Santos-Martins D, Tillack AF, Forli S. AutoDock Vina 1.2.0: New Docking Methods, Expanded Force Field, and Python Bindings. J Chem Inf Model. 2021 Jul 26;61(8):3891-3898. doi:10.1021/acs.jcim.1c00203
11. Genheden S, Ryde U. The MM/PBSA and MM/GBSA methods to estimate ligand-binding affinity. Expert Opin Drug Discov. 2015 Jun;10(5):449-61. doi:10.1517/17460441.2015.1032936
12. Ghetu AF, Corcoran CM, Cerchietti L, Bardwell VJ, Melnick A, Privé GG. Structure of a BCOR corepressor peptide in complex with the BCL6 BTB domain and mapping of the interaction site. Proc Natl Acad Sci USA. 2008;105(11):5357-5362. doi:10.1073/pnas.0800012105
13. Grossfield A, Patrone PN, Roe DR, Schultz AJ, Siderius DW, Zuckerman DM. Best Practices for Quantification of Uncertainty and Sampling Quality in Molecular Simulations. J Chem Theory Comput. 2019 Jan 8;15(1):1-3. doi:10.1021/acs.jctc.8b01072
14. Hatzi K, Melnick A. Breaking bad in the germinal center: how deregulation of BCL6 contributes to lymphomagenesis. Trends Mol Med. 2014;20(8):343-352.
15. Hess B, Bekker H, Berendsen HJC, Fraaije JGEM. LINCS: A linear constraint solver for molecular simulations. J Comput Chem. 1997;18(12):1463-1472. doi:10.1002/(SICI)1096-987X(199709)18:12<1463::AID-JCC4>3.0.CO;2-H
16. Hollingsworth SA, Dror RO. Molecular Dynamics Simulation for All. Neuron. 2018 Sep 5;99(5):833-850. doi:10.1016/j.neuron.2018.08.031
17. Homeyer N, Gohlke H. Binding free energy calculations: MM-PB(GB)SA in practice. Methods Mol Biol. 2012;819:255-76. doi:10.1007/978-1-61779-465-0_17
18. Huang J, Rauscher S, Nawrocki G, Ran T, Feig M, de Groot BL, Grubmüller H, MacKerell AD Jr. CHARMM36m: an improved force field for folded and intrinsically disordered proteins. Nat Methods. 2017 Jan;14(1):71-73. doi:10.1038/nmeth.4067

19. Jo S, Kim T, Iyer VG, Im W. CHARMM-GUI: A web-based graphical user interface for CHARMM. J Comput Chem. 2008;29(11):1859-1865. doi:10.1002/jcc.20945
20. Kerres N, Steurer S, Schluckebier C, Böttcher J, et al. Chemically Induced Degradation of the Oncogenic Transcription Factor BCL6. Angew Chem Int Ed Engl. 2017 Oct 16;56(43):13493-13496. doi:10.1002/anie.201707809
21. Kitchen DB, Decornez H, Furr JR, Bajorath J. Docking and scoring in virtual screening for drug discovery: methods and applications. Nat Rev Drug Discov. 2004;3(11):935-949. doi:10.1038/nrd1549
22. Klebe G. The use of thermodynamic and kinetic data in drug discovery. Nat Rev Drug Discov. 2015 Apr;14(4):231-2. doi:10.1038/nrd4583
23. Kuntz DA, Privé GG. Crystal structure of the BCL6 BTB domain in complex with OICR-4425 (PDB 7LZQ). ACS Med Chem Lett. 2023;14(2):199-210. doi:10.1021/acsmedchemlett.2c00555
24. Lobanov MY, Garbuzynskiy SO, Galzitskaya OV. Radius of gyration is indicator of compactness of protein structure. Biofizika. 2008 Jul-Aug;53(4):623-8. PMID:18856071
25. McCoull W, Cheung T, McAndrew PC, Rowlands T, et al. Discovery of Pyrazolo[1,5-a]pyrimidine B-Cell Lymphoma 6 (BCL6) Inhibitors. J Med Chem. 2017 May 25;60(10):4387-4405. doi:10.1021/acs.jmedchem.7b00306
26. Meng XY, Zhang HX, Mezei M, Cui M. Molecular docking: a powerful approach for structure-based drug discovery. Curr Comput Aided Drug Des. 2011 Jun;7(2):146-57. doi:10.2174/157340911795677602
27. Pagadala NS, Syed K, Tuszynski J. Software for molecular docking: a review. Biophys Rev. 2017 Jun;9(2):91-102. doi:10.1007/s12551-017-0257-1
28. Papaleo E, Saladino G, Lambrughi M, Lindorff-Larsen K, Gervasio FL, Nussinov R. The Role of Protein Dynamics in the Evolution of New Protein Functions. Adv Protein Chem Struct Biol. 2016;94:129-72. doi:10.1016/bs.apcsb.2016.02.002
29. Pinzi L, Rastelli G. Molecular Docking: Shifting Paradigms in Drug Discovery. Int J Mol Sci. 2019 Sep 4;20(18):4331. doi:10.3390/ijms20184331
30. Robustelli P, Piana S, Klein JC, Brangwynne CP, Shaw DE. Developing a molecular dynamics force field for both folded and disordered protein states. Proc Natl Acad Sci U S A. 2018 Jun 5;115(23):E4758-E4766. doi:10.1073/pnas.1720185115

31. Salentin S, Schreiber S, Haupt VJ, Adasme MF, Schroeder M. PLIP: fully automated protein-ligand interaction profiler. Nucleic Acids Res. 2015 Jul 1;43(W1):W443-7. doi:10.1093/nar/gkv315
32. Słabicki M, Yoon H, Koeppel J, et al. Small molecule-induced polymerization triggers degradation of BCL6. Nature. 2021;590:164-168.
33. Sliwoski G, Kothiwale S, Meiler J, Lowe EW. Computational methods in drug discovery. Pharmacol Rev. 2014;66(1):334-395. doi:10.1124/pr.112.007336
34. Trott O, Olson AJ. AutoDock Vina: Improving the speed and accuracy of docking with a new scoring function, efficient optimization, and multithreading. J Comput Chem. 2010;31(2):455-461. doi:10.1002/jcc.21334
35. Valdés-Tresanco MS, Valdés-Tresanco ME, Valiente PA, Moreno E. gmx_MMPBSA: A new tool to perform end-state free energy calculations with GROMACS. J Chem Theory Comput. 2021;17(10):6281-6291. doi:10.1021/acs.jctc.1c00645
36. Wang E, Sun H, Wang J, Wang Z, Liu H, Zhang JZ, Hou T. End-point binding free energy calculation with MM/PBSA and MM/GBSA: principles, applications, and recent advances. Chem Rev. 2019 Aug 28;119(16):9478-9508. doi:10.1021/acs.chemrev.9b00055

Supplementary Files

This is a list of supplementary files associated with this preprint. Click to download.

- SupplementaryInformation1.docx